Supplementary Information

Ratiometric Highly Sensitive Luminescent Nanothermometers Working in the Room Temperature Range. Applications to Heat Propagation in Nanofluids

Carlos D. S. Brites,[a] Patrícia P. Lima,[a] Nuno J. O. Silva,[a] Angel Millán,[b] Vitor S. Amaral,[a] Fernando Palacio[b] and Luís D. Carlos[a] *

[a] Departamento de Física and CICECO, Universidade de Aveiro, 3810–193 Aveiro, Portugal
[b] Departamento de Fisica de la Materia Condensada, Facultad de Ciencias and Instituto de Ciencia de Materiales de Aragón, CSIC–Universidad de Zaragoza, 50009 Zaragoza Spain

METHODS

Synthesis of [Eu(btfa)$_3$(MeOH)(bpeta)], [Tb(btfa)$_3$(MeOH)(bpeta)], Eu(acac)$_3$·3H$_2$O and Tb(acac)$_3$·3H$_2$O complexes. The starting chemicals were europium or terbium chloride hexahydrate ($EuCl_3 \cdot 6H_2O$ or $TbCl_3 \cdot 6H_2O$, Aldrich), 4,4,4-trifluoro-l-phenyl-1,3-butanedione (btfaH, Aldrich), 1,2–bis(4–pyridyl)ethane (bpeta, Aldrich), acetyl acetone (acacH, Aldrich), methanol (MeOH, Merck) and ethanol (EtOH, Fisher). The synthesis procedure of the [Eu(btfa)$_3$(MeOH)(bpeta)] and [Tb(btfa)$_3$(MeOH)(bpeta)] complexes was described in detail elsewhere.[1] The metal (Eu^{3+} or Tb^{3+}) first coordination sphere is formed by three btfa ligands, one bpeta unity and one MeOH molecule (Figure S1a). The Eu(acac)$_3$·3H$_2$O complex was prepared by the addition of an EtOH solution of acacH (0.310×10^{-3} L, 0.3×10^{-3} mol) to an EtOH solution of $EuCl_3 \cdot 6H_2O$ (0.357 g, 0.1×10^{-3} mol) followed by the addition of an aqueous ammonium solution until the pH reaches 6.5. After stirring for 24 h, at room temperature, the solvent was evaporated and the obtained complex dried at 318 K under vacuum. The same method has been adopted for the synthesis of the Tb^{3+} complex, using the corresponding stoichiometric ratio.

The synthetic method adopted for the preparation of the complexes and the data from the elemental analysis and FTIR spectroscopy indicate that the Ln^{3+} first coordination sphere encompasses three acac anionic ligands and three water molecules,[2] Figure S1b.

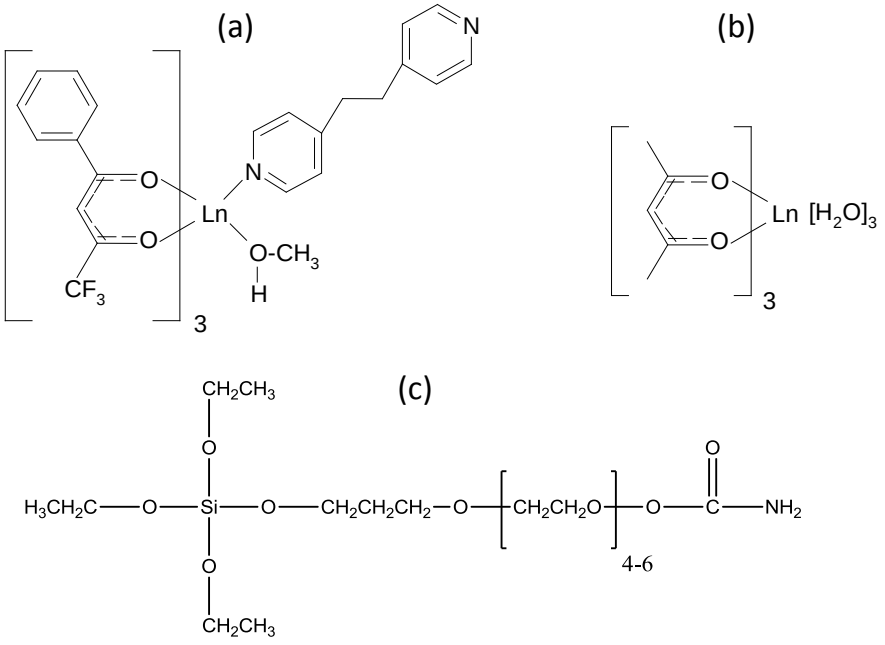

Figure S1. Chemical structure of (a) [Ln(btfa)$_3$(MeOH)(bpeta)]; (b) Ln(acac)$_3$·3H$_2$O (Ln=Eu and Tb) and (c) TESP.

Synthesis of γ-Fe$_2$O$_3$ ferrofluid. Iron oxide nanoparticles were prepared by basic hydrolysis of $FeBr_2/FeBr_3$ aqueous solutions according to the following procedure: an aqueous solution (25×10^{-3} L) containing $FeBr_2$ (6.914 g, 32.058×10^{-3} mol, Aldrich) and $FeBr_3$ (9.475 g, 32.058×10^{-3} mol, Aldrich), was added dropwise to a 1.5 M NaOH (Aldrich) solution (250×10^{-3} L) under stirring at 368 K. The solution was kept under stirring for 30 min, and then cooled down to room temperature. The precipitate was separated by magnetic decantation and then was washed twice by re-dispersion in water and centrifugation. After this, it was re-dispersed

in 0.01 M HCl (500×10^{-3} L). Finally it was separated by centrifugation and then re-dispersed in water.

Synthesis of γ-Fe_2O_3@TEOS/TESP ferrofluid. The silica coating of the γ-Fe_2O_3 NPs was carried out using an acid catalysed silica co-condensation of TEOS and N-(triethoxysilylpropyl)-O-Polyethylene Oxide Urethane (TESP, Figure S1c). In a typical procedure, 1.0×10^{-3} L of γ-Fe_2O_3 ferrofluid was added to 20×10^{-3} L of isopropoxiethanol. The pH of the solution was lowered by addition of 2.0×10^{-3} L of HCl 1M, and 0.2×10^{-3} L of TEOS was added and the solution was stirred during 90 min. Then, 0.20 g of TESP was added at once and after stirring for 150 min, the suspension was placed in a *petri* plate and evaporated at 318 K overnight. The resulting powder sample was labelled as **NP4**.

Synthesis of Eu^{3+}/Tb^{3+}-containing γ-Fe_2O_3@TEOS/TESP NPs. The Eu^{3+}/Tb^{3+} co-doped NPs, named as **NP4-1.3**, were produced using an Eu:Tb ratio of approximately 1:3 adding the [Ln(btfa)$_3$(MetOH)(bpeta)] (Ln=Eu and Tb) solutions (1×10^{-3} L, 6.0 g·L^{-1}) to the reaction medium prior to the addition of the alkoxysilane precursors. The Eu, Tb, Fe and Si content (% w/w) is presented in Table S1.

Synthesis of Eu^{3+}/Tb^{3+}-containing γ-Fe_2O_3@TEOS/APTES NPs. The silica coating of the γ-Fe_2O_3 NPs was carried out using the modified Stöber method. γ-Fe_2O_3 ferrofluid (0.5×10^{-3} L) was added to a solution of isopropoxyethanol (20×10^{-3} L, Aldrich, 99%) and ammonia (2×10^{-3} L, Panreac, 25wt%). This solution was stirred for 30 min and then TEOS (0.2×10^{-3} L, Aldrich, 99.99%), (APTES) (0.4×10^{-3} L, Aldrich, 98%) and Ln(acac)$_3$·3H$_2$O (Ln=Eu and Tb) solutions (1×10^{-3}L, 6.0 g·L^{-1}) were added. The mixture was aged during two hours at room temperature and dried under vacuum to obtain brown powders, named as **NP5-1.4**. The Eu, Tb, Fe and Si content (% w/w) is presented in Table S1.

The pH of **NP4-1.3** and **NP5-1.4** nanofluids (or aqueous suspensions) (1 g·L^{-1}) was measured using a WTW inoLab® pH 720 pH meter. Before any adjustment, the **NP4-1.3** and **NP5-1.4** suspensions present, respectively, pH values of 6.85 and 7.01. Further on, the pH was varying from 4.5 to 7.9 by adding dropwise NaOH (0.1 M) or HCl (0.1 M). Before acquisition of the emission spectra the solutions were stirred during 5 min.

Electron microscopy and dynamic light scattering. Scanning electron micrographs (SEM) of the nanoparticles were obtained using a Hitachi SU-70 FEG-SEM and the chemical composition (and elemental maps) was measured on a Bruker AXS Quantax 400 energy dispersive X-ray spectrometry system (EDS). Transmission electron microscopy (TEM) observations were carried out in a JEOL-2000 FXII microscope. Dynamic Light Scattering (DLS) measurements were performed in a Nanosizer ZS apparatus from Malvern.

Photoluminescence (PL). The low temperature PL measurements were performed using a He closed-cycle cryostat and the temperature was increased with a resistance heater using a Lakeshore 333 auto-tuning temperature controller with a resistance heater. The absolute emission quantum yields were measured at room temperature using a quantum yield measurement system C9920-02 from Hamamatsu with a 150 W Xenon lamp coupled to a monochromator for wavelength discrimination, an integrating sphere as sample chamber and a multi-channel analyzer for signal detection. Three measurements were made for each sample and the average is reported. The method is accurate within 10%.

Scanning temperature measurements. Temperature measurements were performed using a QR450-7-XSR Ocean Optics optical fiber (reflectance/backscattering probe) and an Ocean

Optics S2000 optical detector. A nanomax 3-Axis flexure translation stage from ThorLabs® moves the circuit with steps of 200×10^{-6} m.

The temperature uncertainty δT was estimated for the **NP4-1.3** and **NP5-1.4** nanofluids in the absence of the heating source on the the capillary tube. When converted to absolute temperature, the emission spectra of **NP4-1.3** and **NP5-1.4** correspond to temperature fluctuations of 0.4 K. This value was assumed as the experimental temperature uncertainly of all the temperature measurements. Temperature mappings of the **NP4-1.3** and **NP5-1.4** nanofluids were also recorded with a Flir i50 IR camera (pixel field of view of $250\text{-}350\times10^{-6}$ m, according to the manufacturer). The temperature fluctuations measured in the absence of the heating source on the capillary tube permits to estimate δT as 0.32 degree, compatible to the thermal sensitivity reported by the manufacturer (~0.1 degree). Previously published results using the same IR camera demonstrated that the temperature algorithm makes a significant averaging integrating the information of several pixels.[3] This is evident from the IR camera temperature mapping of an FR4 print-circuit board recovered with a Eu^{3+}/Tb^{3+}-based organic-inorganic hybrid film as the camera cannot distinguish the temperature between two adjacent tracks (depicted as the orange bars in the Figure below).[3]

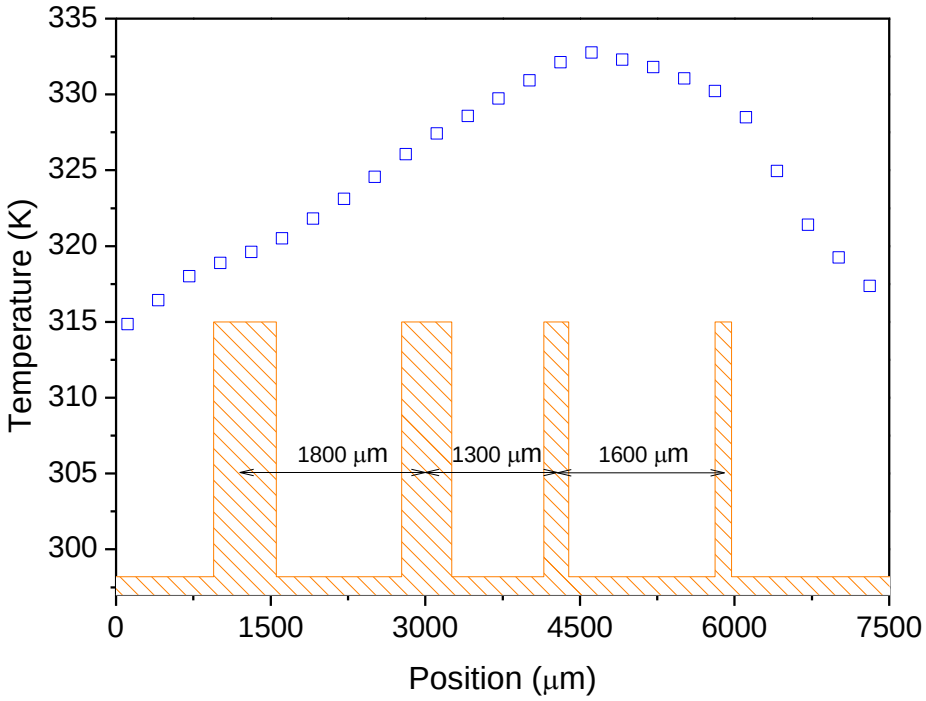

Additionally, the temperature starts to decrease at ~4500×10^{-6} m, before the position of the last track, that presents the highest temperature (narrowest the track, highest the temperature). This indicate that at ~4500×10^{-6} m the temperature algorithm takes into account points located away from the next adjacent track at ~6000×10^{-6} m which should be at a lower temperature. These results point out that the IR camera integrates temperature over, at least, 1500×10^{-6} m, corresponding to an effective field of view of 5-7 pixels.

TEM, DLS AND OPTICAL MICROSCOPY IMAGES

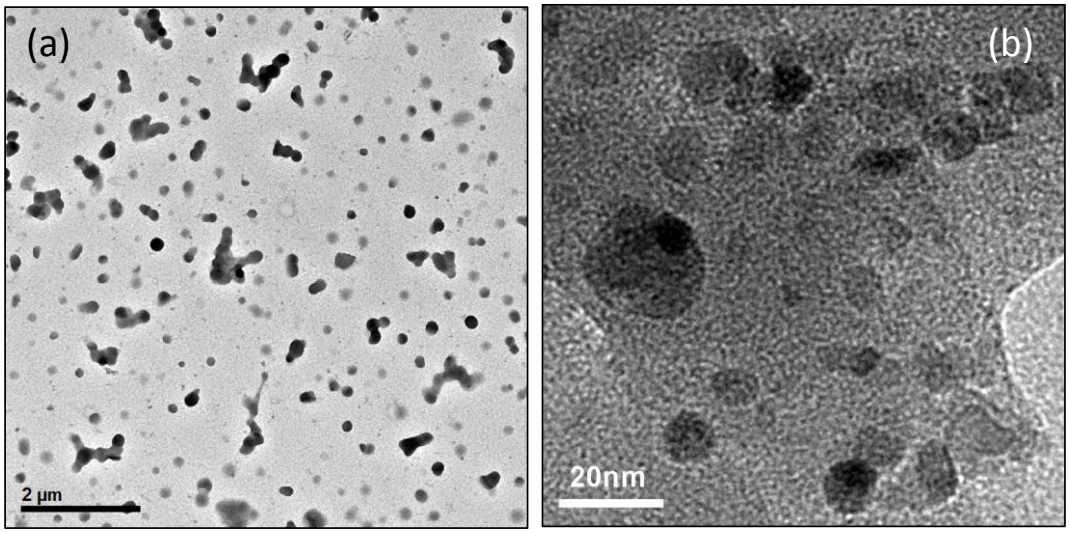

Figure S2. TEM images of **NP4-1.3**. (a) General view of the sample showing the silica beads. (b) Detail of encapsulated iron oxide nanoparticles.

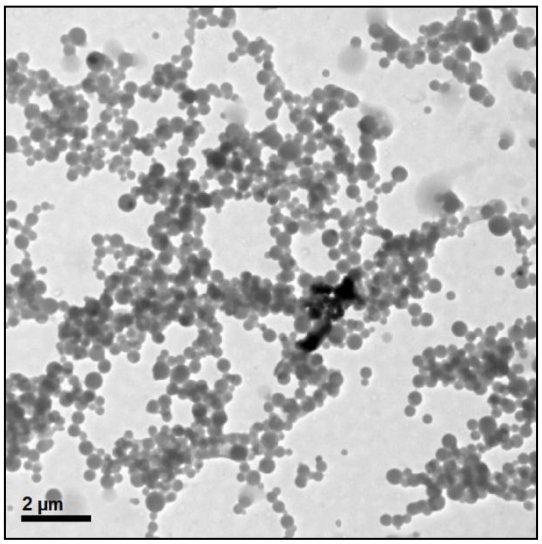

Figure S3. TEM image of **NP5-1.4**: general view of the sample showing the spherical silica beads.

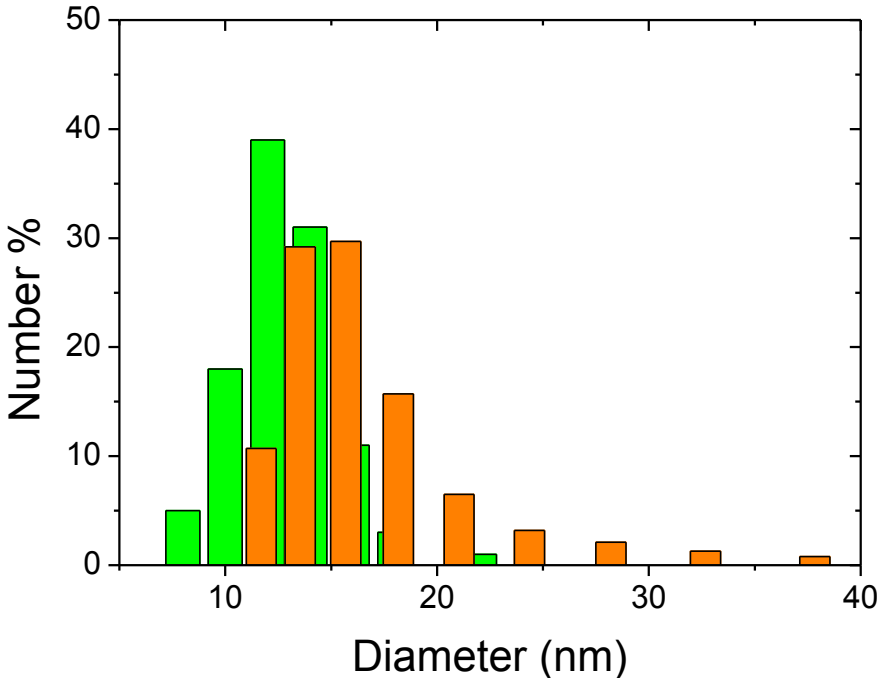

Figure S4. Comparison of the γ-Fe_2O_3 NPs size distribution estimated using TEM images (green) and DLS (orange) measurements.

Since DLS measures the hydrodynamic size of the γ-Fe_2O_3 NPs, the mean size values obtained using DLS (14±3 nm) is slighly higher than that obtained from TEM images (12±2 nm).

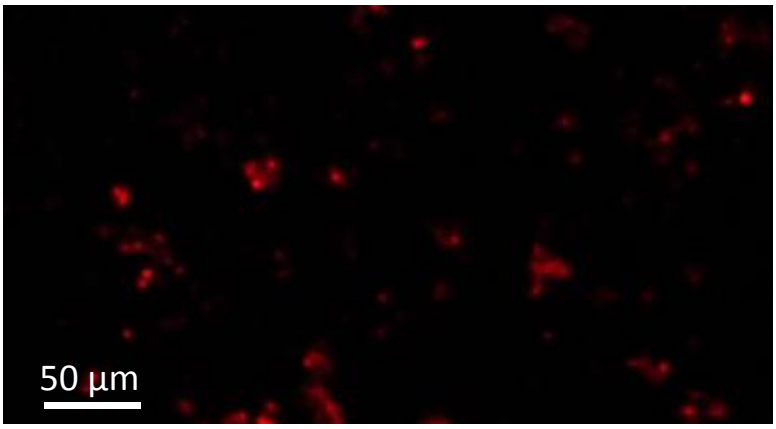

Figure S5. Optical microscopy image of **NP5-1.4** excited at 365 nm using a emission band pass filter (transmission above 95% between 600 and 620 nm) to observe the red emission assigned to the transition $^5D_0 \rightarrow {}^7F_2$ (Eu^{3+},613.5 nm).

PHOTOLUMINESCENCE (FIGURES AND TABLES)

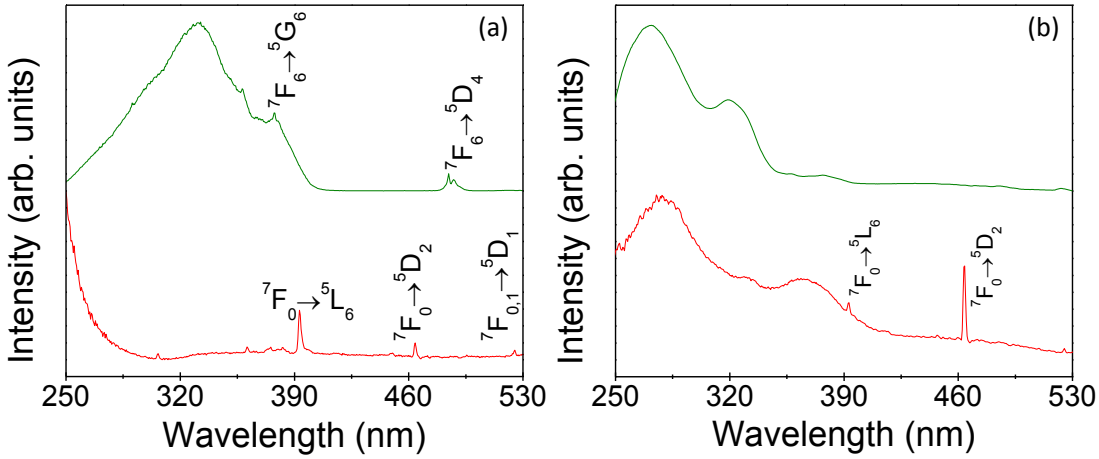

Figure S6. Excitation spectra (300 K) of (a) $Tb(acac)_3 \cdot 3H_2O$, monitored within the $^5D_4 \rightarrow {}^7F_5$ transition (546.5 nm, green line), $Eu(acac)_3 \cdot 3H_2O$, monitored within the $^5D_0 \rightarrow {}^7F_2$ transition (613.5 nm, red line); (b) **NP5-1.4**, monitored within the $^5D_4 \rightarrow {}^7F_5$ (545.0 nm, green line) and the $^5D_0 \rightarrow {}^7F_2$ (611.1 nm, red line) transitions. The spectra were corrected for the spectral distribution of the lamp intensity using a photodiode reference detector.

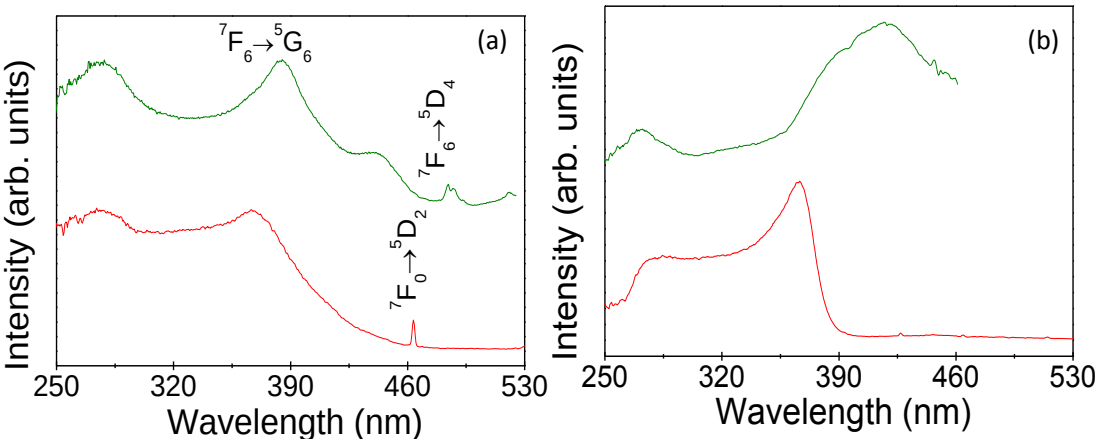

Figure S7. Excitation spectra (300 K) of (a) $[Eu(btfa)_3(MeOH)(bpeta)]$, monitored within the $^5D_0 \rightarrow {}^7F_2$ (612.0 nm, red line) transition, $[Tb(btfa)_3(MeOH)(bpeta)]$, monitored within the $^5D_4 \rightarrow {}^7F_5$ (543.0 nm, green line) transition; and (b) **NP4-1.3**, monitored within the $^5D_0 \rightarrow {}^7F_4$ (700.5 nm, red line) and $^5D_4 \rightarrow {}^7F_6$ (490.5 nm, green line) transitions.

The broad bands in the spectra of $Tb(acac)_3 \cdot 3H_2O$ and $[Eu(btfa)_3(MeOH)(bpeta)]$ are related to the excited states of the acac and btfa/bpeta ligands. In the spectra of **NP4-1.3** and **NP5-1.4** the broad bands ascribed to the excited states of the TEOS/APTES and TEOS/TESP shell are also discerned at ~270 nm and ~280 nm, respectively. The high relative intensity of the ligands–related band with respect to that of the intra-4f lines (quite absent for Tb^{3+} in the spectra of **NP4-1.3** and **NP5-1.4**), indicates a more efficient ligands/host sensitization process, compared with direct intra–4*f* excitation.

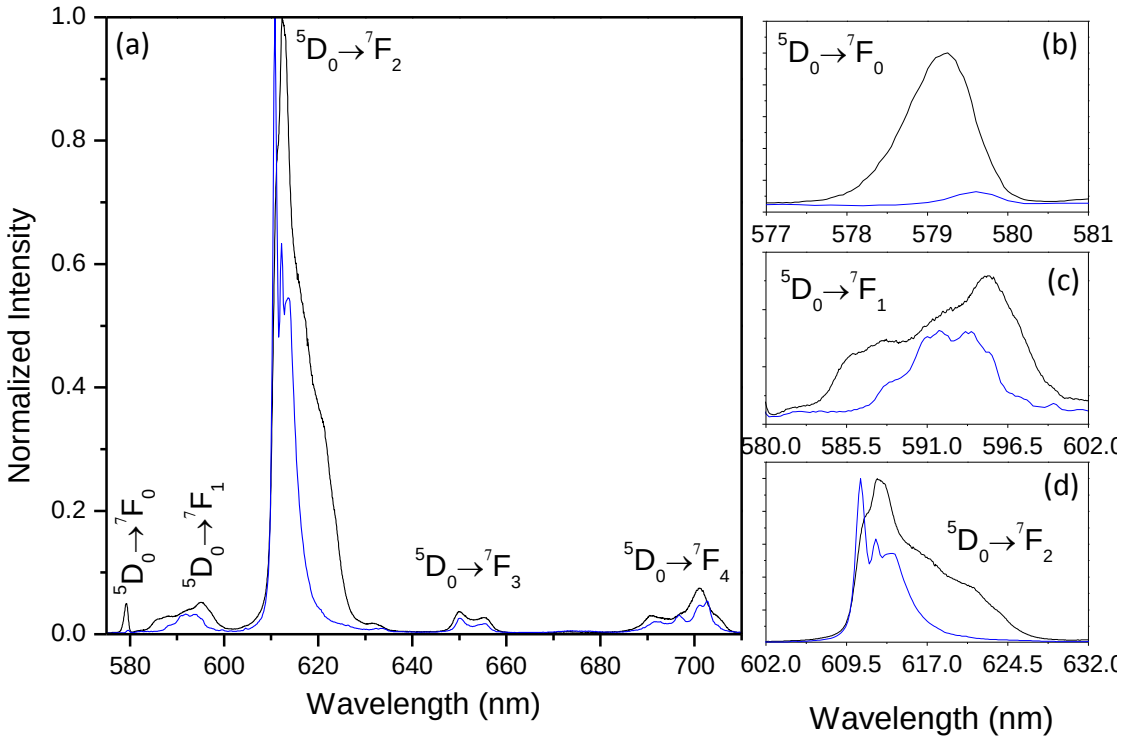

Figure S8. (a) Room-temperature emission spectra of [Eu(btfa)$_3$(MeOH)(bpeta)] (black line), excited at 376.0 nm and **NP4-1.3** (blue line), both spectra excited at 357.0 nm. (b), (c) and (d) are magnifications of the $^5D_0 \rightarrow {}^7F_{0\text{-}2}$ transitions.

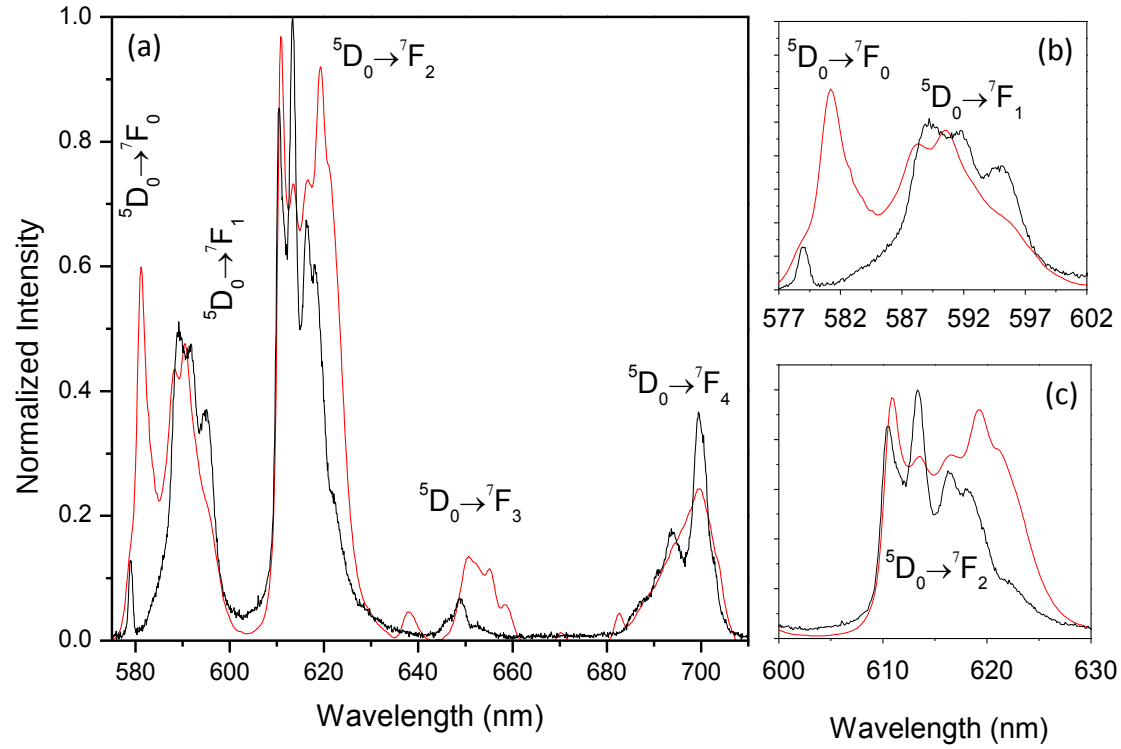

Figure S9. (a) Room-temperature emission spectra of Eu(acac)$_3$·3H$_2$O (black line), excited at 330.0 nm and **NP5-1.4** (red line), excited at 315.0 nm. (b) and (c) are magnifications of the $^5D_0 \rightarrow {}^7F_{0\text{-}2}$ transitions.

The presence of a single $^5D_0 \rightarrow {}^7F_0$ (Eu^{3+}) line, the local field splitting of the $^7F_{1,2}$ levels in three and five Stark components, respectively, and the high relative intensity of the $^5D_0 \rightarrow {}^7F_2$ transition indicate that the Eu^{3+} ions occupy a single low–symmetry local environment (without an inversion center). This is unequivocally supported by the $^5D_0$ and $^5D_4$ decay curves which are well modeled by single exponential functions (Figure S10).

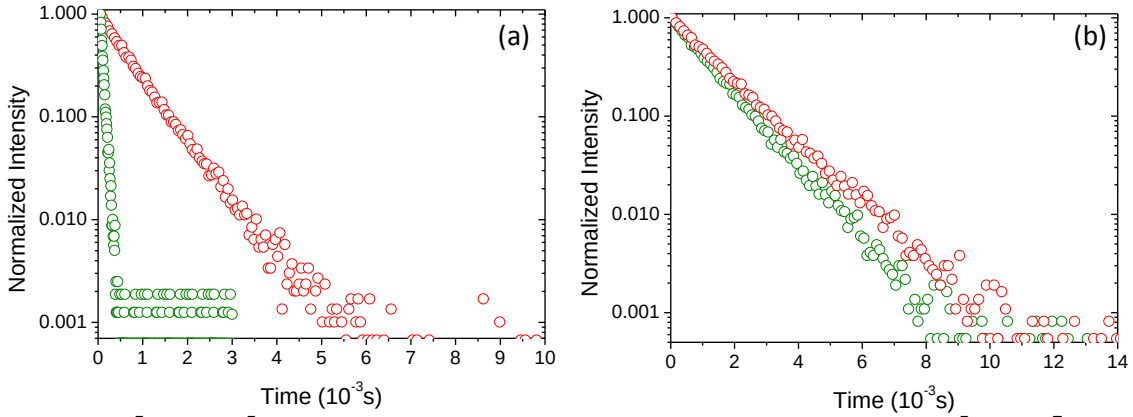

Figure S10. $^5D_0$ and $^5D_4$ decay curves at room-temperature monitoring the $^5D_0 \rightarrow {}^7F_2$ (Eu^{3+}, 613.5 nm) (red) and the $^5D_4 \rightarrow {}^7F_5$ (Tb^{3+}, 546.5 nm) (green) transitions in **NP4-1.3** (a) and **NP5-1.4** (b). The excitation wavelengths are 357 nm (a) and 315.0 nm (b). All the decay curves present linear time dependence in the semi-logarithmic plot indicating that all the excited states lifetimes are well modeled by single exponential functions.

Comparison of the emission features of $[Eu(btfa)_3(MeOH)(bpeta)]$ and $Eu(acac)_3 \cdot 3H_2O$ with those of **NP4-1.3** and **NP5-1.4** shows that the energy, the full width at half maximum (fwhm) and the relative intensities of the $^5D_0 \rightarrow {}^7F_{0-4}$ transitions are strongly altered, indicating an effective interaction between the Eu^{3+} ions and the TEOS/TESP and TEOS/APTES layer, respectively (Figure S5). To quantify further the differences in the emission features between the nanocomposites and the Eu^{3+} complexes, the fwhm and the energy of the $^5D_0 \rightarrow {}^7F_0$ transition were estimated by deconvoluting the emission spectra at 14 K, assuming a single Gaussian function, resulting in the outcome that, the energy of the $^5D_0 \rightarrow {}^7F_0$ transition for **NP4-1.3** (17253.2±9.0 cm^{-1}) and **NP5-1.4** (17205.8±9.0 cm^{-1}) is red shifted in comparison with those estimated for $[Eu(btfa)_3(MeOH)(bpeta)]$ (17266.7±9.0 cm^{-1}) and $Eu(acac)_3 \cdot 3H_2O$ (17272.1±9.0 cm^{-1}), respectively. The corresponding fwhm values are 29.4±1.1 cm^{-1}, 19.4±0.9 cm^{-1}, 26.5±1.0 cm^{-1} and 29.2±1.2 cm^{-1}, for $[Eu(btfa)_3(MeOH)(bpeta)]$, **NP4-1.3**, $Eu(acac)_3 \cdot 3H_2O$ and **NP5-1.4**, respectively.

As reported for similar organic/inorganic hybrids incorporating analogous β-diketonate complexes,[1, 4, 5] we believe that the embedding of the complexes within the γ-Fe_2O_3@TEOS/TESP and γ-Fe_2O_3@TEOS/APTES nanoparticles induces the replacement of the labile MeOH and H_2O molecules, respectively, in the Eu^{3+}–first coordination sphere, thus anchoring the complexes at the particle surface (via the silanol groups or the nitrogen atoms of APTES or TESP). This is supported by the increase in the $^5D_0$ lifetime after the complexes were embedded into the nanoparticles (an increase already reported[4, 6]). At 10 K, for instance, the $^5D_0$ lifetime of $[Eu(btfa)_3(MeOH)(bpeta)]$ and $Eu(acac)_3 \cdot 3H_2O$ are $(0.443\pm0.002)\times10^{-3}$ s and $(0.057\pm0.001)\times10^{-3}$ s, respectively, whereas the corresponding values for **NP4-1.3** and **NP5-1.4** are, respectively, $(0.557\pm0.005)\times10^{-3}$ s and $(0.850\pm0.006)\times10^{-3}$ s (Figure S11). Further, the interaction between the Eu^{3+} ions and the particle surface is inferred by the measurement of the absolute emission quantum yields. The corresponding maximum absolute emission quantum yields, 0.32±0.03, 0.01±0.001, 0.37±0.04 and 0.27±0.03, for

[Eu(btfa)$_3$(MeOH)(bpeta)], Eu(acac)$_3$·3H$_2$O, **NP4-1.3** and **NP5-1.4**, respectively, are listed in Table S2.

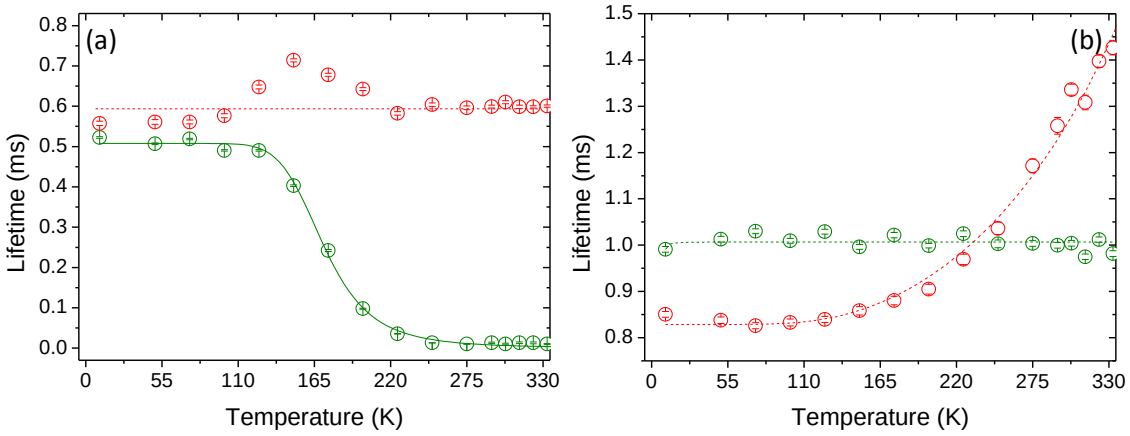

Figure S11. Lifetime dependence in the 10-330 K temperature range of **NP4-1.3** (a) and **NP5-1.4** (b). The dotted lines are guides for the eyes, while the full curve corresponds to the best fit of the experimental data using Equation S2 ($r^2 > 0.998$).

The radiative desexcitation probability of the Tb^{3+} $^5D_4$ level may be approximately described in **NP4-1.3** by the Mott-Seitz model, which expresses the temperature dependence of the experimental lifetime as:[6]

$$\tau^{-1} = \tau_r^{-1} + k\, exp\left(-\frac{\Delta E}{k_B T}\right) \quad \text{(S2)}$$

where τ_r is the radiative lifetime, k is the migration energy rate, ΔE is the activation energy between the triplet host level and the $^5D_4$ state, k_B is the Boltzmann constant and T is the absolute temperature. The activation energy obtained is 1195±15 cm^{-1}.

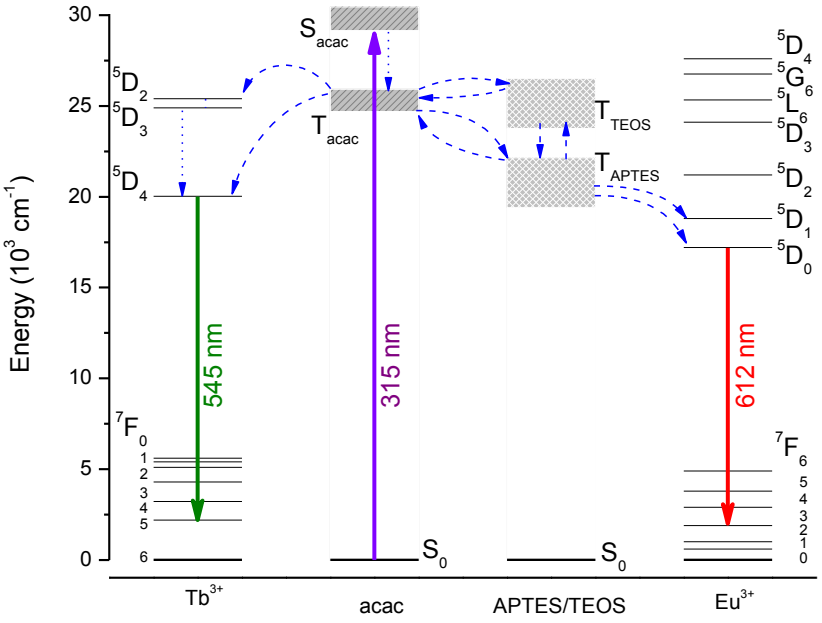

Figure S12. Partial energy level diagram of the **NP5-1.4** nanocomposite. Whereas the doted lines represent the intersystem crossing between the singlet and triple levels of acac and non-radiative decays between the $^5D_2$, $^5D_3$ and $^5D_4$ Tb^{3+} levels, the dashed lines assign the most probable energy transfer processes active above 175 K, *e.g.* acac-to-Tb^{3+}, acac-to-TEOS/APTES, TEOS/APTES-acac and APTES-to-Eu^{3+}. Although possible the TEOS-to-Tb^{3+} ($^5D_{4,2}$)/Eu^{3+}($^5D_4$, $^5G_6$, $^5L_6$) and acac-to-Eu^{3+} ($^5D_4$, $^5G_6$, $^5L_6$) processes are not depicted. The acac-to-Tb^{3+}/Eu^{3+} energy transfer processes are governed by the multipolar mechanism (ΔJ=2, 4, 6), involving the $^5D_{4,2}$ (Tb^{3+}) and $^5D_4$, $^5G_6$, $^5L_6$ (Eu^{3+}) levels and the APTES-to-$^5D_{1,0}$ ones are ruled by the exchange mechanism (ΔJ=0,±1, 0→0 excluded, although the rule is relaxed because of *J*-mixing effects and thermal population of the $^7F_1$ level[7]). The partial energy diagram published by Kai *et al.*[8] was used to depicted the acac and Ln^{3+} energy levels. The APTES/TEOS energy levels (20768±2750 cm^{-1} and 25124±2750 cm^{-1}, respectively) were obtained using the procedure described elsewhere.[9]

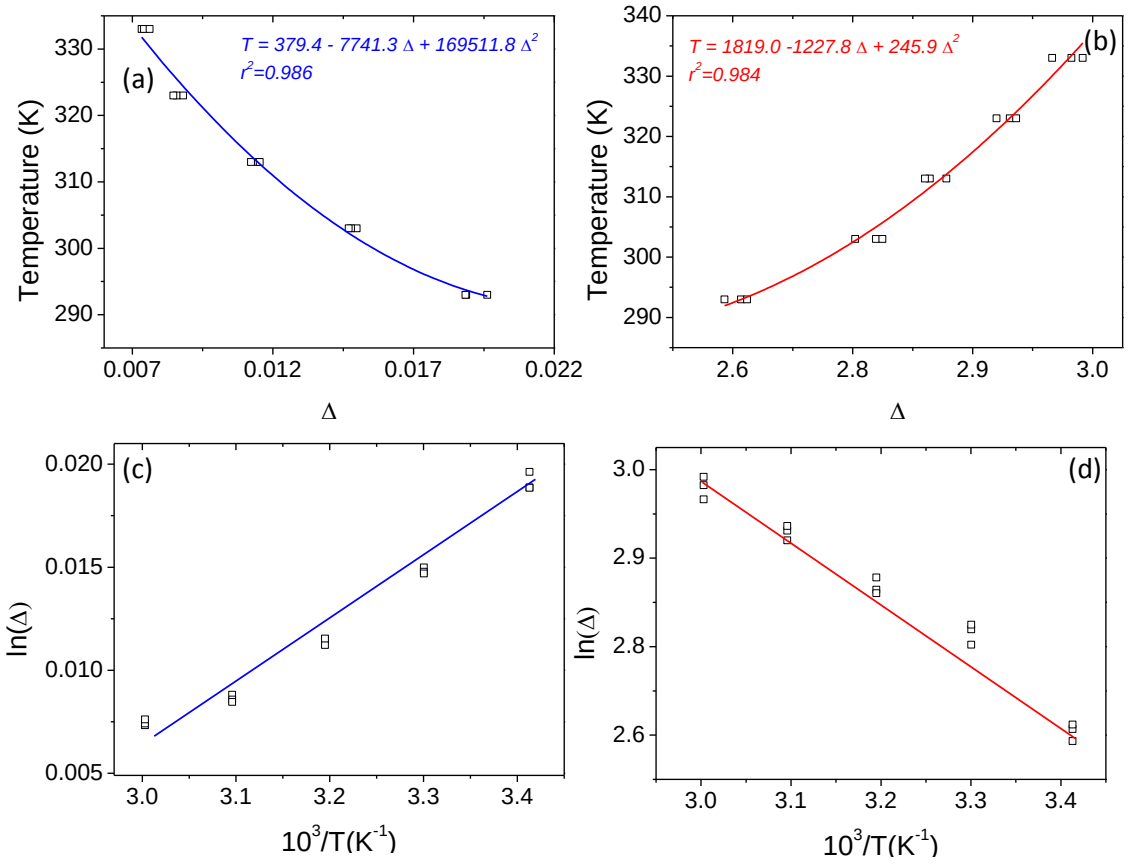

Figure S13. Calibration curves (solid lines) of (a) **NP4-1.3** and (b) **NP5-1.4** in water suspensions (1.0 g·L^{-1}). The temperature was cycled three times and the emission spectra (excited at 360 nm) recorded at equal time intervals when the temperature increases. The results for all cycles (open symbols) are overlapped. (c) and (d) illustrate for **NP4-1.3** and **NP5-1.4**, respectively, the linear dependence of the *ln(Δ)* with the inverse of temperature in the 293–333K temperature range.

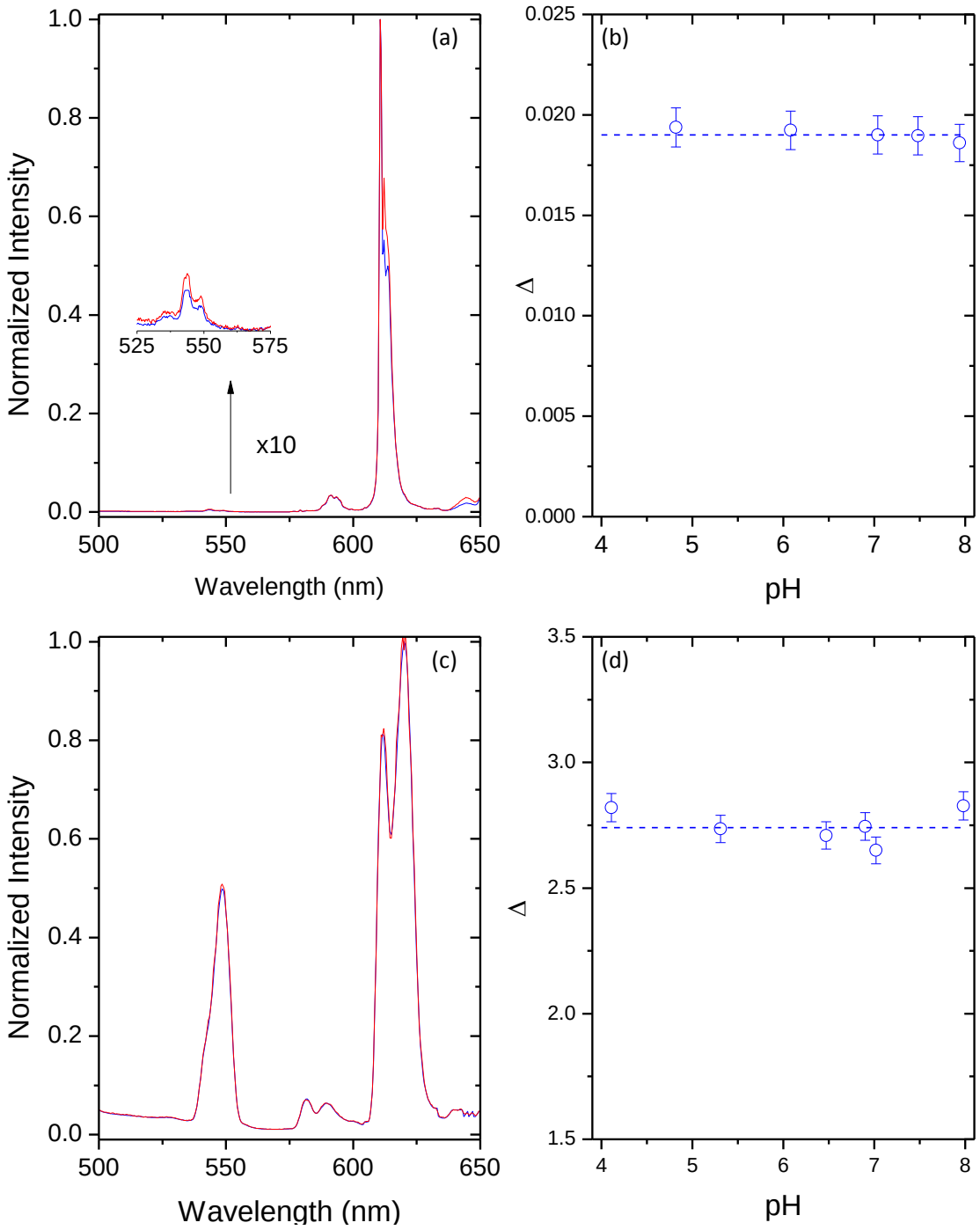

Figure S14. (a) Emission spectra of the **NP4-1.3** aqueous suspension at pH=4.8 (red) and pH=7.5 (blue). (b) Evolution of the thermometric parameter Δ in the pH range 4.8-7.9 of **NP4-1.3**. (c) Emission spectra of the **NP5-1.4** aqueous suspension at pH=4.1 (red) and pH=7.0 (blue). (d) Evolution of the thermometric parameter Δ in the pH range 4.1-8.0 of **NP5-1.4**. All spectra were recorded at 300 K.

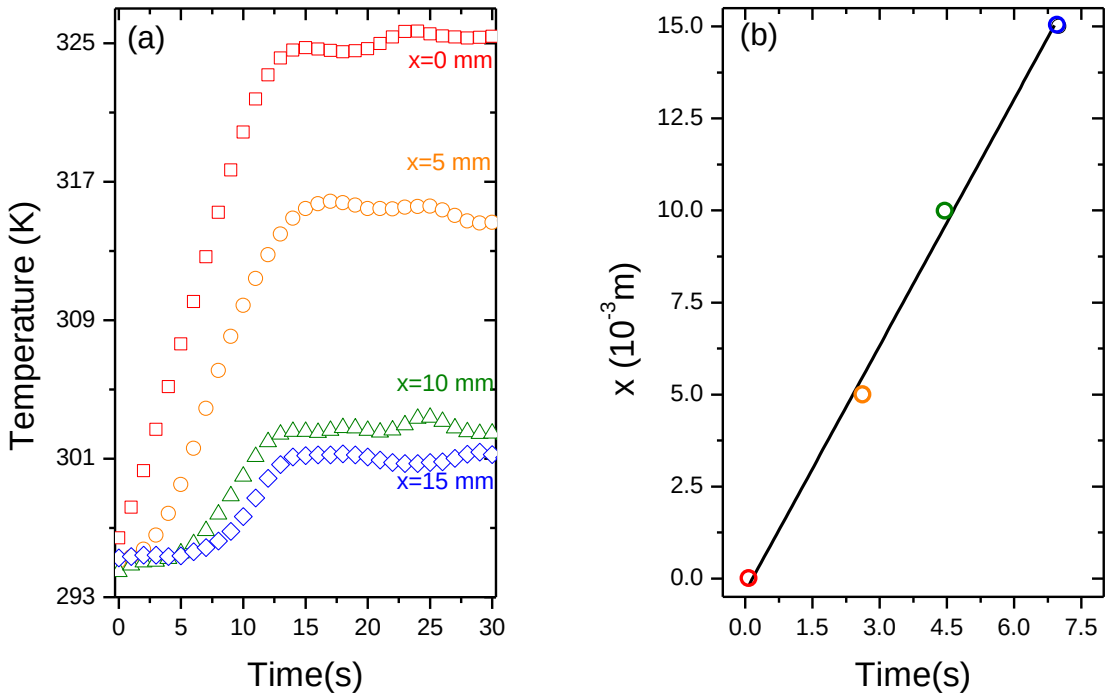

Figure S15. (a) Temperature time evolution of **NP4-1.3** in different points *x* along the capillary tube. (b) Linear relation (r^2=0.995) between the distance *x* travelled by the thermal wave and the time instant t_0 for which the temperature start to increase relatively to the equilibrium value (294 K).

Table S1. Maximum room temperature absolute emission quantum yield values of **NP5-1.4** (315 nm) **NP4-1.3** (357nm) and obtained for the excitation wavelength reported in parenthesis.

Sample	Solid	Water Suspension (1 $g \cdot L^{-1}$)
NP5-1.4	0.27±0.03	0.24±0.02
NP4-1.3	0.37±0.04	0.38±0.04

Table S2. Eu, Tb, Fe and Si elemental analysis (% w/w). The Eu, Tb, Fe and Si content were obtained by inductively coupled plasma optical emission spectroscopy (ICP-OES) analysis on a Jobin Yvon Activa-M instrument with a glass concentric nebulizer. For the Eu and Tb analysis the samples were digested under microwaves with 2×10^{-3} L of nitric acid (HNO_3) and 0.75×10^{-3} L of hydrogen peroxide (H_2O_2). The samples were collected in 25×10^{-3} L flasks and the total volume adjusted using ultrapure water. The method is accurate within 10 %.

Sample	Element			
	Eu	Tb	Si	Fe
NP5-1.4	0.6	2.4	22.9	0.3
NP4-1.3	1.3	4.1	10.2	0.1

MAGNETIC SUSCEPTIBILITY

ac susceptibility was recorded at increasing temperatures (from 5 to 300 K) and selected frequencies of the external excitation field in the 9-852 Hz range, after initial cooling from room temperature down to 5 K in the absence of the field. ac magnetic susceptibility was also recorded at 300 K as a function of frequency from 0.1 to 1103 Hz. All measurements were performed on a MPMS-XL (Quantum Design) magnetometer.

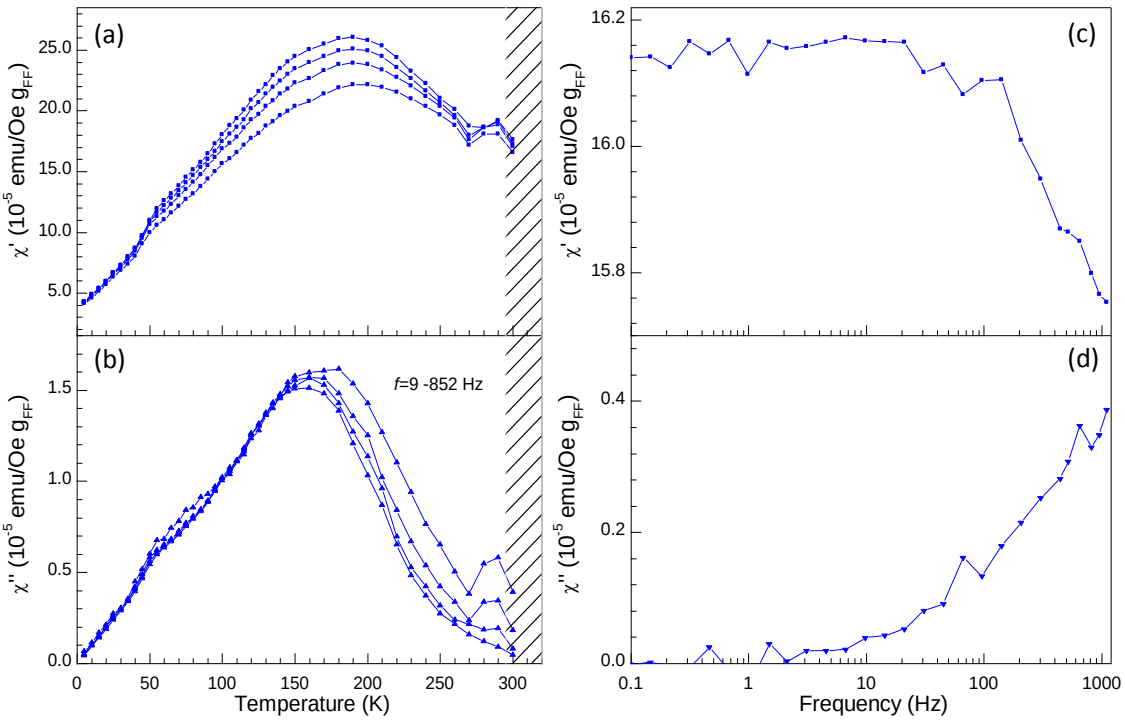

Figure S16. (a) Temperature dependence of the in phase component χ' at selected frequencies of the external ac magnetic field (in the 9 to 852 Hz range). (b) Temperature dependence of the out of phase component χ''. Frequency dependence (300 K) of (c) χ' and (d) χ''.

The temperature dependence of the ac magnetic susceptibility is typical of superparamagnetic nanoparticles undergoing an unblocking process as temperature increases. At low temperature, the magnetic moment of the nanoparticles is freeze in a given direction being unable to overcome the anisotropy energy barrier and follow the external ac field, resulting in a frequency dependence of the in phase component of the magnetic susceptibility χ' and in the existence of and out of phase component χ''. Below the freezing point of water, the magnetic moment of the nanoparticles can overcome the anisotropy energy barrier and relax only by thermally activated processes (termed Néel relaxation). Above the freezing point of water, the all nanoparticle is able to rotate and follow the external ac field by Brownian processes. The onset of this Brownian motion results in the increase of both χ' and χ''.

The existence of χ'' is associated to the dissipation of energy in the form of heat, being the base of magnetic hyperthermia.[10] In the linear response regime, the specific loss power associated to the application of one cycle of an external ac field to the magnetic nanoparticles is proportional to $\chi'' fH^2$ where f and H are the frequency and the amplitude of the external ac field, respectively. Therefore, the existence of a non zero χ'' component shows that the maghemite nanoparticles used in the nanothermometers behave as local heat sources when excited with an external ac magnetic field in the all studied temperature range and in particular at room temperature.

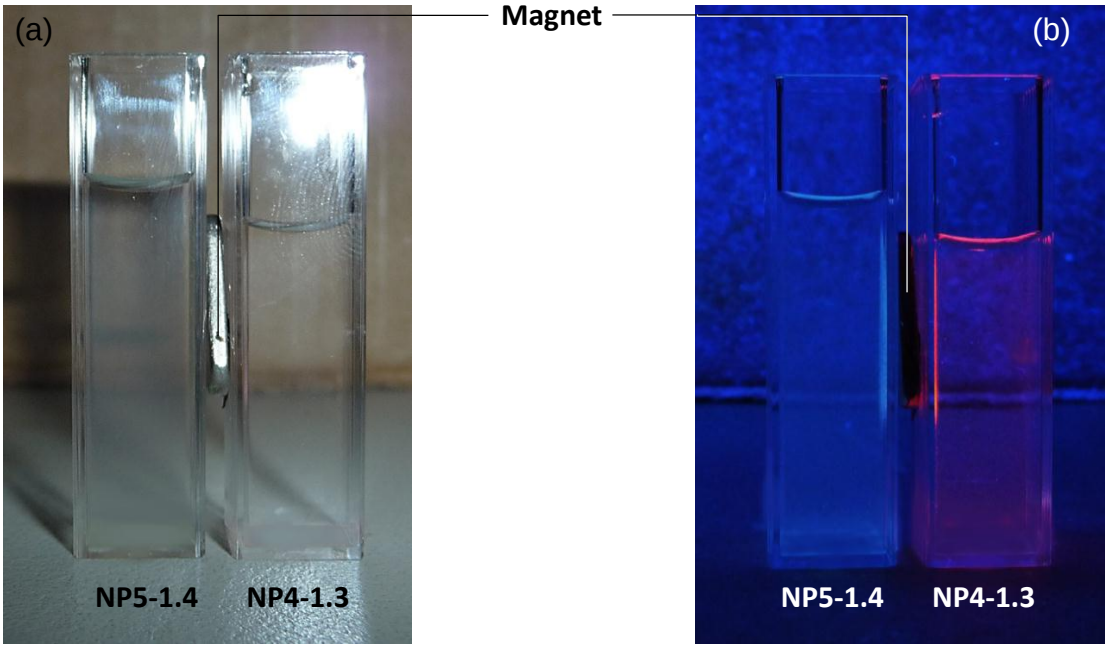

Figure S17. Photographs of the **NP4-1.3** and **NP5-1.4** nanofluids ($1g \cdot L^{-1}$) under laboratory daylight (a) and 365 nm UV light (b) illumination. The magnetic capture of the bifunctional magnetic-optical nanoparticles induced by a small commercial magnet is clearly discernible in (b).

REFERENCES

1. C. D. S. Brites, P. P. Lima, N. J. O. Silva, A. Millán, V. S. Amaral, F. Palacio and L. D. Carlos, *Adv. Mater.*, 2010, **22**, 4499-4504.
2. P. P. Lima, R. A. S. Ferreira, S. A. Junior, O. L. Malta and L. D. Carlos, *J. Photochem. Photobio. A-Chem.*, 2009, **201**, 214-221.
3. C. D. S. Brites, P. P. Lima, N. J. O. Silva, A. Millán, V. S. Amaral, F. Palacio and L. D. Carlos, *J. Lumin.*, 2013, **133**, 230-232.
4. P. P. Lima, F. A. A. Paz, R. A. S. Ferreira, V. de Zea Bermudez and L. D. Carlos, *Chem. Mater.*, 2009, **21**, 5099-5111.
5. P. P. Lima, R. A. S. Ferreira, R. O. Freire, F. A. A. Paz, L. S. Fu, S. Alves, L. D. Carlos and O. L. Malta, *Chem.Phys.Chem.*, 2006, **7**, 735-746.
6. L. D. Carlos, R. A. S. Ferreira, J. P. Rainho and V. De Zea Bermudez, *Adv. Funct. Mater.*, 2002, **12**, 819-823.
7. P. P. Lima, S. S. Nobre, R. O. Freire, S. A. Junior, R. A. S. Ferreira, U. Pischel, O. L. Malta and L. D. Carlos, *J. Phys. Chem. C*, 2007, **111**, 17627-17634.
8. J. A. Kai, M. C. F. C. Felinto, L. A. O. Nunes, O. L. Malta and H. F. Brito, *J. Mater. Chem.*, 2011, **21**, 3796-3802.
9. C. D. S. Brites, V. T. Freitas, R. A. S. Ferreira, A. Millan, F. Palacio and L. D. Carlos, *Langmuir*, 2012, **28**, 8190-8196.
10. R. E. Rosensweig, *J. Magn. Magn. Mater.*, 2002, **252**, 370-374.